SSRG International Journal of Electrical and Electronics Engineering
ISSN: 2348-8379/ https://doi.org/10.14445/23488379/IJEEE-V12I6P110

Volume 12 Issue 6, 125-135, June 2025

Original Article

Physics-Informed Analytical Framework for Design and Optimization of a Dual-Radius Spherical Antenna Array under Mutual Coupling

Oluwole John Famoriji[1], Thokozani Shongwe[2]

[1,2]*Department of Electrical and Electronic Engineering Technology, University of Johannesburg, P.O. Box 524, Auckland Park, Johannesburg 2006, South Africa.*

[1]*Corresponding Author : famoriji@mail.ustc.edu.cn*

Received: 07 April 2025 Revised: 09 May 2025 Accepted: 08 June 2025 Published: 30 June 2025

Abstract - *Developing high-performance antenna arrays for next-generation wireless systems necessitates precise control over radiation characteristics, mutual coupling effects, and spatial configurations. An effective antenna array configuration for examining the spatial characteristics of Electromagnetic (EM) fields is spherical antenna arrays (SAAs). However, the physical properties of the array ultimately determine how well SAA-based signal processing algorithms operate. In particular, the array's size, the elements' angular positions, and other variables affect the frequency range over which an SAA offers good spatial information. In contrast to traditional designs, this research explores the design of SAAs that provide a broader frequency range of operation, and elements are dispersed on and away from the surface of a rigid spherical array to achieve this. At first, a general framework for modeling SAAs with elements positioned at different distances from the origin of the array and for calculating optimal filters to decompose the EM wave into spherical harmonic modes is presented. Additionally, an optimization technique is proposed for developing multi-radius SAAs that considers the total number of components and the intended spatial resolution to accomplish an optimally wide frequency range of operation. In addition, a proof-of-concept dual-radius SAA prototype with 64 components is designed based on the optimization results. A comparison between the theoretical predictions and the measurements for the prototype SAA is conducted, and the results obtained are good enough to support the implementation of the proposed framework in practical EM engineering. For instance, this work lays a foundational step toward developing compact, high-gain antenna arrays for emerging applications in 5G/6G communications, satellite systems, and wireless sensor networks.*

Keywords - *Spherical antenna arrays, Beamforming, Antenna arrays, 3D signal representation, Signal data acquisition.*

1. Introduction

The Spherical Antenna Arrays (SAAs) have garnered significant attention in recent research [1-7], proving particularly effective for receiving electromagnetic waves (EM) in specific scenarios. Their symmetric nature provides an excellent framework for examining electromagnetic fields in the spherical harmonic (SH) domain. SH signal processing has been used in several fields during the last ten years, such as beamforming [5], source localization and separation, [6], signal reconstruction [4], and design consideration analysis [7]. The high elevation and azimuth estimate accuracies can be obtained simultaneously with a spatially symmetrical spherical array. How the elements are distributed determines the spherical array configuration; for instance, positioning sensors on the vertices of platonic solids produces a uniform spherical array. Additionally, the SAA data is subjected to SH decomposition for SH domain representation, making it easier to express the received signal in terms of components dependent on time, frequency, and location. Unlike fixed beamformers, which apply a constraint to a particular look direction and optimize the filter weights concerning performance measures like white noise gain, sidelobe levels, or the directivity index, signal-dependent beamformers optimize the filter weights while accounting for signal and noise characteristics. We typically need an estimate of the noise Power Spectral Density (PSD) matrix in order to calculate the weights of signal-dependent beamformers. However, in reality, the noise signals cannot be seen. Hence, estimating the noise PSD from the noisy signals is necessary. Inspired by single-channel techniques to noise PSD estimation, previously proposed spatial domain noise estimators based on the signal presence probability (SPP) [8, 9] aim to update the noise PSD estimate solely in time-frequency bins where there is no signal. The effectiveness of an SH signal processing technique depends on the SAA's capability to deliver accurate observations of the SH modes of the EM field. Specifically, the performance of an SAA (as shown in Figure 1(a), and (b) can be assessed based on its highest spatial resolution and operational bandwidth. Within the SH framework, the SH order determines the narrowest beamwidth that a beamformer can direct, which is known as spatial resolution. The bandwidth of operation is the frequency range throughout which a specific spatial resolution may be maintained with acceptable noise levels. An SAA's physical characteristics, such as its size, the number and positioning of its antennas, the existence of interference, and the situation of its radiators, all affect its performance [3].

(a)

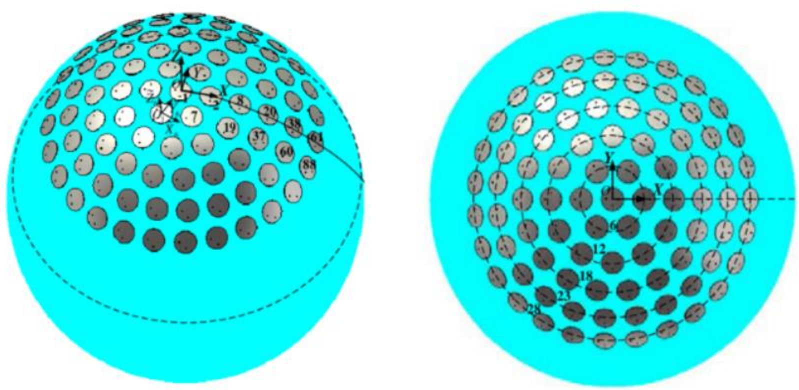

(b)

Fig. 1 Typical spherical antenna array (a) SAA with 64 elements for a conformal demonstration, and (b) geometry of SAA with 88 elements.

This study aims to design SAAs with a constant spatial resolution over the broadest frequency range. In order to broadcast and receive 3D signals in good quality, wideband SAAs are quite desirable. These SAAs are useful for signal processing in the SH domain or for applications that call for directional EM field characterization [5, 6]. For example, consistent spatial resolution across frequencies in EM field imaging is advantageous. Despite the extensive study in SAA signal processing [8-15], relatively few studies have focused on the physical architecture of SAAs to expand their operating bandwidth. In order to record a wider frequency range, previously used two successive open spherical antenna arrays: a bigger array for low frequencies and a smaller array for high frequencies. An issue frequently arises with open arrays is that the perceived signal energy for particular harmonic modes drastically decreases at frequencies dictated by the array radius. By mounting a rigid SAA to a rigid spherical baffle, this problem can be minimized. Meyer and Elko [8] showed that their stiff structure performed better and had a wider operating bandwidth than an equivalent open spherical array.

Alternatively, several open SAAs with different radii can be built concentrically and employed at the same time, and [8]. This allows the EM field to be detected across a wider frequency range and decreases signal energy loss at inconsistent frequencies. As demonstrated in earlier research [9-14], to expand the frequency range of a rigid SAA at low frequencies, an alternate tactic is to add a second layer of elements spaced apart from the rigid baffle.

Typically, the positions of the rectifier antenna and the transmitting source are not fixed. Furthermore, most reported rectifier antennas can only receive RF power in a specific direction, making omnidirectional capability essential for efficient RF energy reception [9]. To achieve better omnidirectional RF energy reception, multisector rectifier antennas using RF energy combining [10] and DC combining [11, 12] techniques have been proposed. The DC combining technique allows the receiving antenna to capture RF energy over a wide beam range [13], making it a promising approach for designing omnidirectional rectifier antennas. A four-sector wireless power transfer (WPT) system has been studied to enhance angular coverage [14]. For further improvement, a six-sector column surface rectifier antenna has been proposed [15, 16].

An integrated eight-sector WPT system operating at 5.8 GHz has also been introduced [17]. Optimization of the array excitation distribution has also been proposed to enhance the beamwidth and improve antenna reception [18]. However, when the incident wave's propagation direction is at the back of the receiving antenna, the antenna can capture only minimal RF energy.

The third type of sampling procedure uses the radiation matrix's properties to identify sampling positions. For instance, sample points are chosen to reduce the radiation matrix's mutual coherence in order to guarantee the best reconstruction performance [19]. In their information-theoretic analysis of the radiation matrix, Behjoo et al. [20] calculated the number of samples needed in each cluster by calculating the maximum energy of the vector SH that makes up the radiation matrix.

They then used frame theory to determine the sampling locations. Furthermore, in light of the radiation matrix's numerically low-rank property, Zhao et al. [21] suggested an adaptive near-field sampling method that uses row skeletonization of the radiation matrix to identify the important sample locations. However, these methods are only appropriate for single-probe sampling systems because they pinpoint specific sampling areas. Array-probe sampling devices are frequently used in practice for spherical near-field measurements, making conventional techniques non-applicable. To overcome these challenges, researchers have utilized the sparsity of band-limited SH of electromagnetic fields to achieve under-sampling in the azimuth, or φ dimension [22, 23]. However, spherical wave coefficients are not inherently sparse, making these methods unsuitable for antenna sampling when dealing with non-sparse coefficients.

In practice, the antenna profile deviates from the ideal surface design, presenting as a curved surface affected by various errors. This discrepancy can lead to a decline in the antenna's electrical performance, representing a common structural-electromagnetic field coupling issue [24, 25]. The current growth and development in technology require a larger array (including many elements), leading to mutual coupling and consequently causing impedance mismatch, poor radiation pattern, and polarization. This problem cannot be avoided in practice. Hence, this work incorporates the effect of mutual coupling. In this study, the challenge of enhancing the operational bandwidth of an SAA is revisited. The highest SH order that can be achieved is increased by adding more radiators to the spherical baffle's surface, but the frequency range across which these signals can be reliably received is still constrained. Thus, we investigate the design of multi-radius SAAs, which are SAAs with parts placed at different distances from the centre. The following is a summary of this work's main innovations and contributions.

a) The impacts of measurement noise, radiator placement inaccuracy, and spatial aliasing are all considered while developing a realistic model for replicating multi-radius SAAs. Furthermore, a framework for figuring out SH decomposition filters that combine the outputs of various radiators in the best possible way is provided.
b) In addition, a technique for designing multi-radius SAAs as efficiently as possible for a specific number of radiators and SH order is presented. This approach greatly enhances the work in [10] by leveraging the structure from (a). Additionally, optimization results are shown for SAAs with rigid baffles surrounded by two, three, and four layers of components. We designed a dual-radius SAA prototype (Figure1(a)) (in proof-of-concept) with 64 elements based on these optimization results (Figure 1(a)).
c) Finally, the prototype's calibration measurement is presented, and the proposed model's predictions are contrasted with the SAA's measured (from simulated SAA) performance. This incorporates the effects of mutual coupling. For an SAA with an arbitrary scattering structure, we also demonstrate the use of calibration measurements to compute SH decomposition filters.

2. SAA with Multi-Radius

2.1. Modeling Antenna Array

This subsection presents the derivation of the model from the knowledge of mathematics and employed in the simulation of the EM behavior of an SAA. A scenario in which an SAA composed of N omnidirectional antennas positioned at different locations around a perfectly rigid sphere with a radius of R is considered. Based on Figure 2, the location of the antennas is defined by spherical coordinates (r, θ, φ). To make it simple and easy, the derivation of the models is made in the frequency domain based on dimensionless frequency kR, where k represents wave number, $k = {}^{2\pi f}/_{c}$, f is the frequency, and c is the speed of the EM wave. Furthermore, for a particular radii distance, r, a dimensionless radius, δ, is introduced.

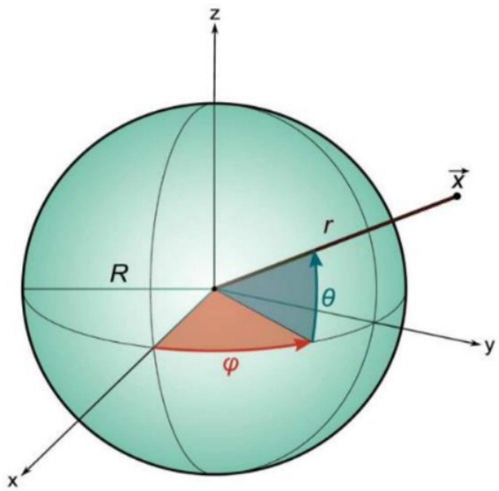

Fig. 2 Illustration of the geometry of SAA

Considering the n-th antenna of SAA having spherical coordinates of $(\delta_n R, \theta_n, \varphi_n)$. For a scenario where the arriving EM field is made up of waves, the pressure quantified by the radiator is expressed as

$$p_n = \sum_{l=0}^{\infty} \sum_{m=-l}^{l} w_l\,(kR, \delta_n) Y_l^m(\theta_n, \varphi_n) b_{l,m}, \qquad (1)$$

Where $b_{l,m}$ The complex coefficient depends solely on the incident sound field, denoted by the SH component with order l and degree m. Y_l^m represents the real-valued spherical harmonic function of order l and degree m and is given as

$$Y_l^m(\theta_n, \varphi_n) = \sqrt{\frac{2l+1(l-m)!}{4\pi\,(l+m)!}} P_l^{|m|}(sin\theta) \ldots \times \begin{cases} \cos m\varphi \ \ for\ m \geq 0 \\ sin|m|\varphi \ \ for\ m < 0' \end{cases} \qquad (2)$$

Where $P_l^{|m|}$ Is the associated Legendre polynomial of order l and degree m. Note that this term arises from the spherical coordinate convention used in this paper (as in Figure 2). $w_l(kR, \delta_n)$ is the 'modal strength' of the order l spherical harmonic modes at the antenna location and is given by

$$w_l(kR, \delta_n) = i'\left(j_i(\delta_n\, kR) - \frac{j_l'(kR)}{h_l^{(2)}(kR)} h_l^{(2)}(\delta_n\, kR)\right), \qquad (3)$$

Where j_i and $h_l^{(2)}$ Denote the spherical Bessel function of order l and the second-kind spherical Hankel function, respectively. We call the Bessel-weighted SH expansion of the electromagnetic pressure Equation (1). The term "spherical Fourier transform" occasionally describes this equation in EM engineering literature. The precise number of EM pressure is calculated by adding up an unlimited number of terms based on Equation (1). This total needs to be reduced for numerical estimation. The truncation order is determined given that the incident electromagnetic field is made up of a unit amplitude plane wave originating from the same axis as the antenna. The expression for the SH components is

$$b_{l,m} = Y_l^m(\theta_n, \varphi_n)\ \forall l\ \in\ \mathbb{N}, m\,\epsilon\,[-l, l]. \qquad (4)$$

Putting $b_{l,m}$ In Equation (1), it becomes

$$p_n = \sum_{l=0}^{\infty} \sum_{m=-l}^{l} w_l\,(kR, \delta_n) Y_l^m(\theta_n, \varphi_n)^2 = \sum_{l=0}^{\infty}(2l+1) w_l(kR, \delta_n), \qquad (5)$$

Hence, the relative error within pressure originating from truncating the series at order L is

$$\epsilon_{l,n}(kR) = \left|1 - \frac{\sum_{l=0}^{L}(2l+1)w_l(kR,\delta_n)}{\sum_{l=0}^{\infty}(2l+1)w_l(kR,\delta_n)}\right|. \qquad (6)$$

The denominator of Equation (6) above has an infinite series. This is approximated using terms up to order 500. Figure 3 displays the approximate truncation error as a function of each truncation order for various values of δ_n Moreover, $kR=22$ corresponds to a frequency of 12 MHz for a spherical array with a radius of 20 cm. A higher truncation order is required for precise pressure calculation the further the antenna is from the sphere's origin. Consequently, the radiators that are farthest from the middle must be taken into account when calculating the truncation order necessary for an SAA to be accurately modeled,

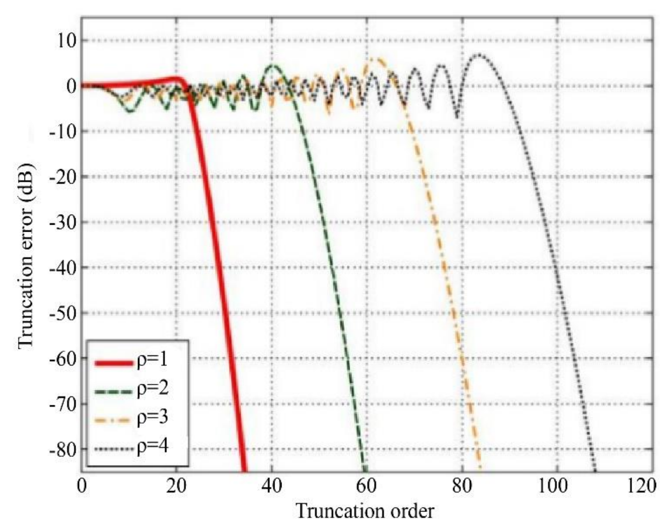

Fig. 3 The truncation error as a result of the truncation order is derived from Equation (6) for various values of δ and *kR*=20

Such that the relative error in the pressure measured by the SAA's farthest element is less than -90 dB (0.01%) for various values of δ, Figure 4 displays how truncation order, Λ, depends on *kR*. Because [·] is the ceiling function, the resulting values of the truncation order vary from those provided by the most commonly utilized truncation order formula in the scientific literature, L= ⌈kr⌉ [4]. In this case, applying this approach would yield a truncation error of roughly 0 dB.

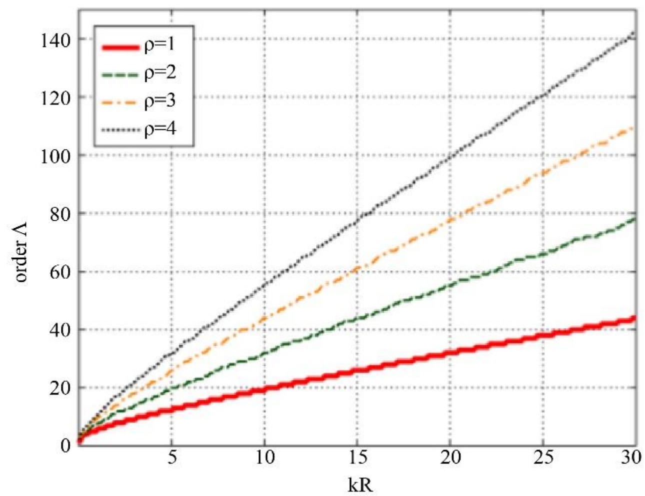

Fig. 4. Plot of truncation order Λ as a function of kR for various values of δ

Assuming that a suitable truncation order, Λ, is established, the EM pressure that the n-th element measures can be expressed as

$$p_n \approx \sum_{l=0}^{\Lambda} \sum_{m=-l}^{l} w_l\,(kR, \delta_n) Y_l^m(\theta_n, \varphi_n) b_{l,m}, \qquad (7)$$

Hence, Equation (7) can be expressed in vector product form as

$$p_n = t_{\Lambda,\mathrm{n}}^T b_\Lambda, \qquad (8)$$

Where

$$t_{\Lambda,n} = \left[t_{0,0,n}, t_{1,-1,n,} t_{1,0,n}, \dots, t_{\Lambda,\Lambda,n}\right]^T,$$
$$t_{\mathrm{l},m,n} = w_l(kR, \delta_n) Y_l^m(\theta_n, \varphi_n),$$
$$b_\Lambda = \left[b_{0,0}, b_{1,-1}, b_{1,0}, \dots, b_{\Lambda,\Lambda}\right]^T \qquad (9)$$

In the same vein, the vector of the received EM pressures by the N antennas constituting the SAA is given as

$$P = T_\Lambda b_\Lambda, \qquad (10)$$

T_Λ denotes the matrix (transfer) that exists between the spherical harmonic components of order Λ and the received pressure by the N antennas, and it is expressed as

$$T_\Lambda = \left[t_{\Lambda,1}, t_{\Lambda,2}, \dots, t_{\Lambda,N}\right]^2. \qquad (11)$$

2.2. SAA Performance Heading

The performance of an SAA design is largely determined by the accuracy with which signals can be retrieved from the EM wave, which is frequency-dependent. This section outlines the factors that limit the performance of an SAA and discusses methods for estimating this performance.

Three main types of mistakes limit a SAA's performance. First, the weights w_l Corresponding to the spherical components could be modest at low kR values. As noted above, whenever the encoding filters are computed without regularization, this leads to a large number of measurement noise in the coded electromagnetic signals. On the other hand, the encoded EM wave's amplitude could be less than the real EM signal once regularization is used. In another way, some electromagnetic signals are not encoded at low frequencies because the SAA cannot detect them properly. The lowest limit of the SAA's operating frequency range is established by this phenomenon: the further the antennas are from the center of the structure, the lower the frequency range.

Spatial aliasing is the second source of mistakes influencing the SAA's performance. Above the spatial-aliasing frequency, which is the frequency at which the distance between an antenna and its closest neighbour equals half a wavelength, spatial aliasing mostly takes place. The SAA is unable to discriminate between high- and low-order electromagnetic wave constituents in the receiving signal within this frequency range. Consequently, noise from high-order constituents contaminates the low-order encoded electromagnetic signals. The maximum limit of the SAA's operating frequency range is the spatial-aliasing frequency. This restriction is directly proportional to the array size: the greater the frequency at which clean electromagnetic signals may be obtained, the nearer the antennas are to the centre.

The antennas' incorrect positioning or calibration is the third cause of errors. Encoding errors arise when the factual transfer matrix is used. T_Λ It differs from the one used to compute the encoding filters due to errors in the radiators' position, gain, or phases. Spatial aliasing may also be affected by mismatches in position or gain. One potential remedy is measuring the antenna array's response for various source orientations. Although these measurements can enhance performance, they cannot provide precise information on the transfer matrix. T_ΛAlternatively, achieve accurate calibration.

We use a stochastic approach to simulate the functionality of an SAA and consider these various causes of error. V sets of antenna locations with a particular average positioning error are generated randomly for a particular antenna array design. After calculating the pressure detected by the antennas for these V sets of SAAs for F plane-wave directions, the pressure values are supplemented with random noise. The vector, $\hat{\boldsymbol{y}}_{\boldsymbol{L},\boldsymbol{f}}^{(v)}$Of the up-until order-L encoded signals that correspond to the f-th plane-wave direction and the v-th set of radiator positions is provided by

$$\hat{y}_{L,f}^{(v)} = E_L\left(T_\Lambda^v y_{\Lambda,f} + \eta^{(v)}\right), \quad (12)$$

The T_Λ Matrix for the v-th set of random antenna placements is denoted by T_Λ^v. For the plane waves originating from direction (θ_n, φ_n), the vector of the signal elements is $y_{\Lambda,f}$, i.e.

$$y_{\Lambda,f} = \left[Y_0^0(\theta_f, \varphi_f), Y_1^{-1}(\theta_f, \varphi_f), \ldots, Y_\Lambda^\Lambda(\theta_f, \varphi_f)\right]^T. \quad (13)$$

Since $\eta^{(v)}$ If it is a randomly generated vector, measurement noise is likely present. A Gaussian distribution is used to generate the vector elements, and the vector is normalized to fix its energy in relation to the average energy that the antennas receive.

After the SAA has been used to encode the EM signals, the signal-to-noise ratio (SNR) can be aggregated over all source locations and sets of element locations as

$$SNR_{(dB)} = 10\, log_{10}\left(\frac{1}{VF}\sum_{v=1}^{V}\sum_{f=1}^{F}\frac{\|y_{L,f}\|^2}{\left\|y_{L,f}-\hat{y}_{L,f}^{(v)}\right\|^2}\right). \quad (14)$$

The output of the order L spherical beamformer $s(\theta_f, \varphi_f, \theta_u, \varphi_u)$ When a plane wave is coming from a direction (θ_f, φ_f) is

$$s(\theta_f, \varphi_f, \theta_u, \varphi_u) = \frac{1}{(L+1)^2}\, y_{L,you}^T y_{L,f}^{(v)}, \quad (15)$$

Where the steering direction is $(\theta_u, \varphi_{you})$. The directivity index (DI) is an important indicator of the SAA's beamforming characteristics [15]. The DI in the proposed model is computed in the same vein as the SNR and is provided as

$$DI_{(dB)} = 10\, log_{10}\left(\frac{1}{VF}\sum_{v=1}^{V}\sum_{f=1}^{F}\frac{\left\|y_{L,f}^T\hat{y}_{L,f}^{(v)}\right\|^2}{\frac{1}{U}\sum_{u=1}^{U}\left\|y_{L,f}\hat{y}_{L,f}^{(v)}\right\|^2}\right). \quad (16)$$

The degree of robustness to measurement noise is a crucial characteristic in antenna array processing, and this aspect is evaluated by computing the white noise gain (WNG). The beamformer's output noise power is divided by the antenna signals' measurement noise power, which is known as the WNG. WNG is calculated using

$$WNG_{(dB)} = 10\, log_{10}\left(\frac{1}{VF}\sum_{v=1}^{V}\sum_{f=1}^{F}\frac{\left\|y_{L,f}^T\hat{y}_{L,f}^{(v)}\right\|^2}{\left\|y_{L,f}^T E_L\right\|^2}\right). \quad (17)$$

3. Designing SAA with Dual-Radius

Using another approach, this part develops design guidelines based on performance limitations. The SAA's design is specifically assessed to find the widest range of frequency of operation for a given number of antennas and spatial resolution. Among the possible designs considered are multi-radius SAAs, which consist of a "rigid" SAA with antennas scattered across the surface of a rigid sphere and a maximum of three "open" SAA layers with antennas located on the surfaces of open spheres of varying radii surrounding the rigid array. We start by examining a dual-radius SAA's performance.

3.1. Analysis of SAA with Dual-Radius

We present the simulation of the SNR of the encoded EM waves for 3 different SAA layouts in Figure 5: "rigid" SAA, which has antennas on the surface of a rigid sphere of radius R; "open" SAA, which has antennas 3R from the centre of the sphere (δ=3); and "dual." SAA, which combines both open and rigid arrays. In the simulations, Three percent of the sphere radius was chosen as the mean element positioning error, or approximately 1 mm when R is 3 cm. The relative measurement noise was set to 30 dB, and the β value was set at 0.05 (dB) (α=20 dB).

The SNR for each value was calculated by averaging 162 plane-wave directions and 20 antenna placements, corresponding to the vertices of an icosahedron refined by many triangulations. The bandwidth of operation for the array is the frequency range in which the SNR of each of the encoded electromagnetic signal components is at least 20 dB.

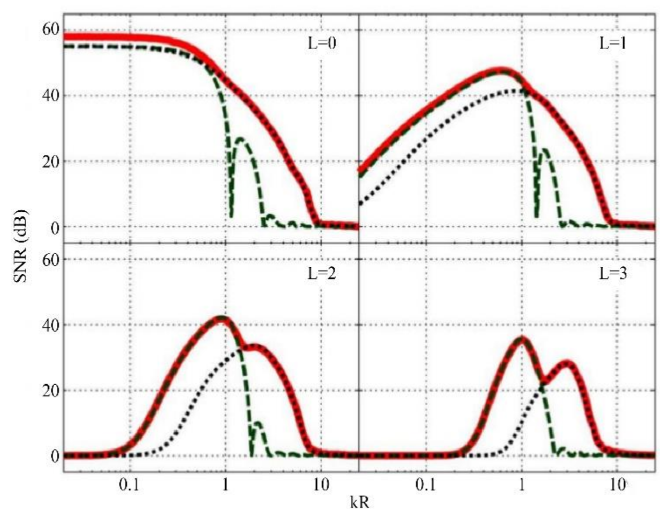

Fig. 5 The SNR simulation of the encoded EM waves is displayed as frequency-dependent for EM orders zero through three (from upper left to lower right). The line types indicate the various antenna configurations: solid line for the merging of these 2 arrays; dashed line for 32 antennas placed at a distance d from the centre of the rigid sphere of radius R; and dotted line for 32 antennas on the surface of the sphere

The three SAAs' performances differ greatly from one another. Because of their sizes, the rigid arrays perform better at higher frequencies than the open arrays at lower frequencies. The frequency range of the rigid array is marginally wider than that of the open array. This disparity arises because the higher frequency limit of the rigid array is determined by spatial aliasing, while the higher frequency limit of the open array is affected by an uneven frequency at order 0. The SNR of the dual array is comparable to or higher than the SNRs of the rigid and open arrays when they are taken separately, the dual array's frequency range is larger than the total frequency ranges of the rigid and open arrays, and the SNR of the dual array-encoded signals is 6 dB higher than the rigid and open arrays for order 0 and low frequencies.

The order-0 EM signal at low frequencies is simply averaged over twice as many radiators due to the proportional contributions of the rigid and open arrays, which reduces the measurement noise level by 6 dB.

3.2. Optimizing SAA with Dual-Radius

Out of all the conceivable multi-radius SAA designs, this subsection discusses creating the configuration that provides the broadest range of functioning frequency for EM wave order zero to three. Simplifying how to describe the actual construction, the optimal dual-radius SAA design is initially phased. Conversely, the proposed approaches can be generalized to solve all multi-radius challenges, as illustrated below. Please assume that the open and stiff arrays' spherical surfaces have an equal distribution of their elements. Three characteristics define the Dual-radius SAA design: The symbol δ indicates the ratio of the rigid and open arrays' radii, whereas N_{open} and N_{rigid} These are the number of elements comprising the open and rigid array. Additionally, We ensure that the total number of elements in the array, $N_{open} + N_{rigid}$, equals 64. The SAA setup is, therefore, fully described by δ and N_{open}. In the optimization process, each N_{open} Value is examined to identify the ideal value δ and the resulting operating frequency range.

From order 0 to order 3, the SAA's operational bandwidth is the width of the frequency range where the EM wave elements' SNR is at least 20 dB. N_{open} It should be from 16 to 48 for both rigid arrays and the open arrays to encode the EM waves of order 3 since there are 16 EM wave components for orders 0 through 3. Therefore, for $N_{open} < 16$, the dual-radius SAA's operational range is the same as the rigid array's, which does not depend on δ. The dual radius functional range of SAA is the same as with the open array, regardless of δ, for $N_{open} > 48$.

The ideal figure of δ_{opt} for the radius (non-dimensional) is estimated to be the highest dimensionless radius with a range of $\mathrm{N_{open}}$ From 16 to 48. This is so that when kR ranges between $\mathrm{kR}_{\max}^{(\mathrm{open})}$ and $\mathrm{kR}_{\max}^{(\mathrm{rigid})}$, where $\mathrm{kR}_{\max}^{(\mathrm{open})}$ Is the value of kR at maximum SNR order 3 EM waves encoded via the open array only, and $\mathrm{kR}_{\max}^{(\mathrm{rigid})}$ Denotes the kR at maximum SNR of order 3 EM waves encoded by utilizing the open array only. The following gives the methodical Algorithm that shows how the δ_{opt} is calculated.

Algorithm: Calculation

Initialization: $\delta_1 = 1; \delta_2 = 100.$
Calculate $\mathrm{SNR}^{(\mathrm{rigid})}$ for $KR \in [0, 10]$.
Estimate $KR_{max}^{(\mathrm{rigid})}$.
while $\delta_2 \geq 1.05\ \delta_1$ do
    $\delta \leftarrow \sqrt{\delta_1 \delta}.$
    Calculate $\mathrm{SNR}^{(\mathrm{open})}$ for $KR \in [0, 10]$.
    Estimate $KR_{max}^{(\mathrm{open})}$.
    Calculate $\mathrm{SNR}^{(\mathrm{dual})}$ for $KR \in [KR_{max}^{(\mathrm{open})}, KR_{max}^{(\mathrm{rigid})}]$.
    if $\exists\ KR$ such that $\mathrm{SNR}^{(\mathrm{dual})} \leq 20$ dB then
        $\delta_2 \leftarrow \delta.$
    else
        $\delta_1 \leftarrow \delta.$
    end if
end while
$\delta_{opt} \leftarrow \delta_1.$

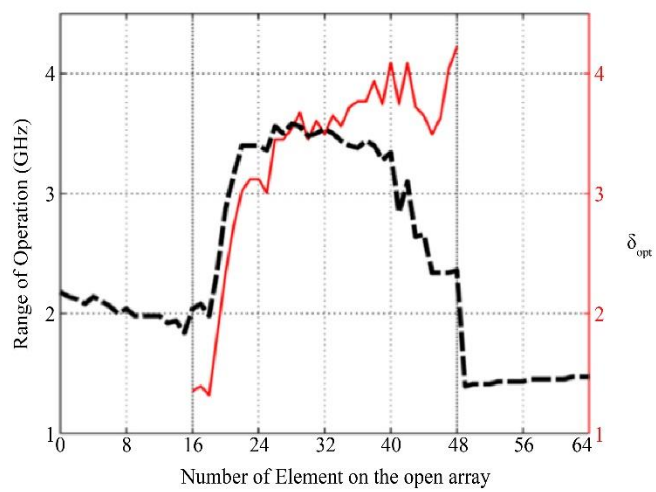

Fig. 6 The plot of the results of the optimization procedure. The thick dotted line on the left axis, which also shows the antenna's number in the open array, shows the range of operating frequency of the SAA. The equivalent ideal radius value δ_{opt} (right axis), with no dimension, is represented by a thin solid line.

The results of the above-described design of SAA and optimization procedure are shown in Figure 6. Using designs with between 22 and 40 antennas on the open array results in wider operating bandwidths. The rigid and open arrays' behaviors combine to produce a frequency range for the designs. This demonstrates a greater range than a rigid design with 64 rigid sphere surface pieces.

In this case, the ideal values for the radius ratio fall between 3 and 4. This illustrates the advantages of a rigid design over an open one. In contrast to the open SAA, which has its limit due to the zeros of the modal strength functions, the rigid SAA's higher frequency limit is produced by spatial aliasing. Compared to an open array, the results demonstrate that a multi-radius SAA performs better with a rigid array at the origin.

4. Analysis of SAA with Dual-Radius in Proof-of-Concept

A dual-radius SAA prototype was designed using the findings of the optimization procedure outlined in the preceding section. Figure 7 shows a picture of this SAA. The rigid array comprises 64 omnidirectional antennas spaced out on a rigid spherical with a radius of 28 mm. 64 omnidirectional antennas make up the outer array, which is mounted on the surface of an open sphere with a radius of 98.4 mm. The arrays' relative sizes were determined to yield a value of δ of 3.4, marginally lower than the optimal value of 3.5 resulting from the optimization.

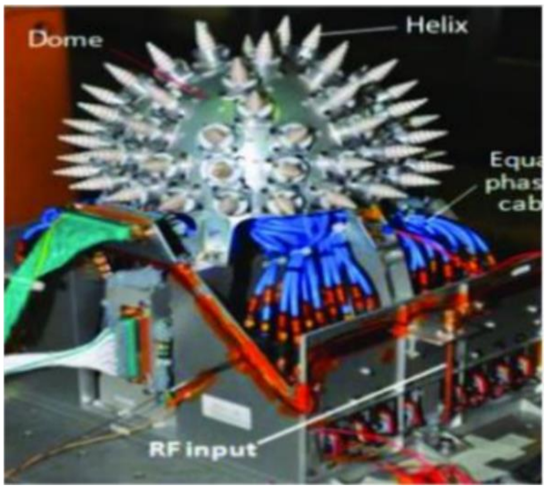

Fig. 7 Picture of SAA used for illustration

4.1. Measurement Campaign

Two sets of calibration tests were carried out in order to assess the SAA prototype's performance. Initially, for frequencies higher than 10 GHz, the SAA was placed in an anechoic chamber with an injection loss of 40 dB. Laser pointers were used to align the SAA at the geometric center of the chamber.

The logarithmic sweep technique was used to quantify the impulse responses for each 585 places where the source was rotated around the antennas (for more information, see [15]). With the restriction that the robotic arm could not reach altitudes below -50 degrees, the source points were dispersed uniformly over the sphere. The spacing between the source and the SAA's origin was roughly one meter for each measuring direction. According to [22], the measurement-based encoding filter is as follows.

4.2. Performance Analysis of SAA Prototype with Dual-Radius

When the order L spherical beamformer is guided toward (θ_u, φ_u), the frequency response between the source at (θ_f, φ_f) And the output is,

$$\rho_{L,u,f} = \frac{1}{(L+1)^2} y_{L,u}^T \, \tilde{E}_L g_f. \tag{18}$$

Sharing similarity with the DI in Equation (16) The average measured DI can be computed using

$$\widetilde{DI}_{(dB)} = 10 \log_{10}\left(\frac{1}{F}\sum_{f=1}^{F} \frac{\|\rho_{L,f,f}\|^2}{\frac{1}{U}\sum_{u=1}^{U}\|\rho_{L,u,f}\|^2}\right). \tag{19}$$

Similarly, when an EM wave encoding filter is used with measurement dependence, the WNG of an order L spherical beamformer is written as,

$$\widetilde{WNG}_{(dB)} = 10 \log_{10}\left(\frac{1}{F}\sum_{f=1}^{F} \frac{\|(L+1)^2 \rho_{L,f,f}\|^2}{\|y_{L,f}^T \tilde{E}_L\|^2}\right) \tag{20}$$

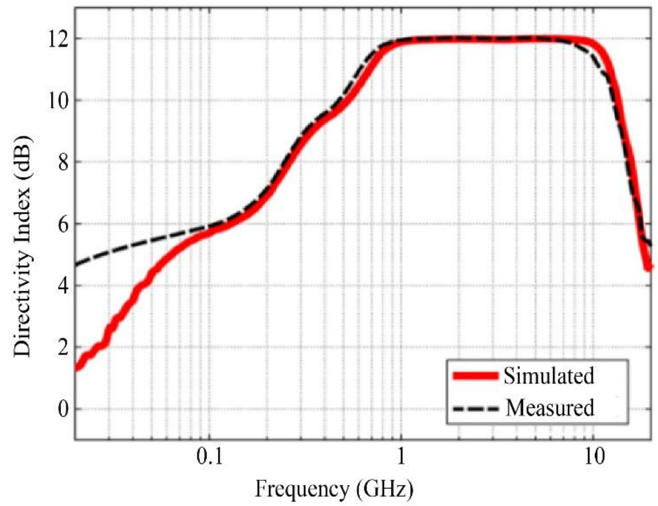

Fig. 8 The simulated (solid line) and measured (dashed line) order-3 DIs versus frequency

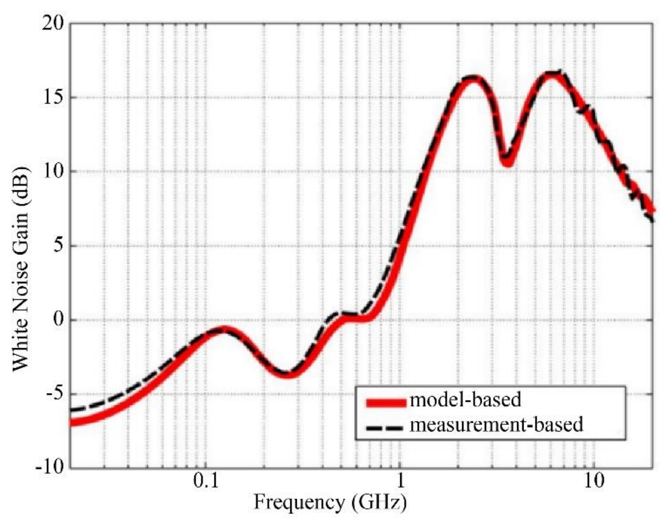

Fig. 9 WNG of order 3 beamformer vs frequency for the measurement-dependent and model-based encoding filters

The computed DI via the model described in Section II and the DI derived from the SAA prototype measurements, as indicated in Equation (19), are compared in Figure 8. The two curves generally fit each other well. The main distinction is that, at frequencies lower than 1 GHz, the measured DI is noticeably higher than the model predicts. This discrepancy results from the fact that the measured frequency responses of the SAA were substituted with theoretical ones in this frequency range that eliminated measurement noise or placement error, whereas the computer models included these sources of error. Furthermore, compared to the simulated DI, the DI obtained from measurement seems slightly biased towards lower frequencies. The action of the structure holding up the outer antennas is probably what caused this movement.

This structure functions as a somewhat absorbent sphere at low frequencies, boosting the presence of high EM wave orders and making the outer array more directional. On the other hand, the structure reflects and diffracts incoming waves at high frequencies, increasing the degree of spatial aliasing and decreasing the directiveness of the inner array. Furthermore, the WNG of the order-3 spherical beamformer derived with model-based encoding filters and obtained with measurement-based filters are compared in Figure 9.

The nearly perfect match between the two graphs indicates that the sensitivity to measurement noise generated by the two filters is nearly equal. This structure functions as a somewhat absorbent sphere at low frequencies, boosting the existence of high EM wave orders and rendering the outer array more directional. On the other hand, the architecture reflects and diffracts incoming radiation at high frequencies, increasing the degree of spatial aliasing and decreasing the directiveness of the inner array.

Furthermore, the WNG of the order-3 beamformer derived with an encoder filter that is model-based and that obtained with measurement-based filters are compared in Figure 9. The nearly perfect match between the two graphs indicates that the sensitivity to measurement noise produced by the two filters is nearly equal.

5. Conclusion and Future Direction

In conclusion, this article presents a framework for analysing, designing, and optimising dual-radius SAA. The outlines of a numerical model that models the electromagnetics of this kind of SAA are given. It presents how to compute encoding filters based on the spherical Fourier transform and predict performance. The design specifications for a dual-radius rigid SAA that provides the broadest frequency range for a specific SFT order are found using this numerical model and an optimization technique.

A 64-element prototype dual-radius SAA was built and calibrated using the optimization results. This prototype's measured performance closely matches what the numerical model predicted. Despite being unique to dual-radius SAAs, the optimization procedure described in this study can be readily applied to antenna arrays with any number of radii, SFT order, or the total of radiators.

Lastly, the proposed method shows that putting certain antennas away from spherical surfaces in rigid form greatly increases the range of frequency of the SAA, whereas commercially available SAAs usually use omnidirectional antennas on the rigid sphere's surface. Comparing the theoretical predictions with the measurements from the prototype SAA, a good match was observed, consequently motivating the implementation of the proposed framework in practical scenarios. The proposed method finds application in various communication technologies.

Developing a physics-informed analytical framework for designing and optimising a dual-radius spherical antenna array opens multiple avenues for future research and practical advancement. As the current model demonstrates promising capabilities in capturing the complex electromagnetic interactions and spatial characteristics inherent to dual-radius configurations, several future directions can further enhance its utility and performance:

a) Incorporating physics-informed neural networks (PINNs) and surrogate modelling could accelerate the optimization process by learning from simulation data while preserving physical constraints. This hybrid approach may significantly reduce computational costs associated with full-wave simulations.
b) Future work can focus on extending the analytical framework to support wideband and multiband antenna designs. This would require accounting for frequency-dependent behavior in the electromagnetic model and optimizing the array geometry accordingly.
c) Research could explore real-time adaptive reconfiguration of the antenna elements based on operational requirements or environmental feedback. A physics-informed framework can be the foundation for developing intelligent control algorithms for beam steering and null formation in dynamic environments.
d) Further analytical development could focus on improving the framework's ability to model and mitigate mutual coupling effects, particularly in dense array configurations. Incorporating advanced decoupling network models or novel array element designs may yield more robust performance.
e) Translating the analytical insights into physical prototypes will be a crucial next step. Building and testing scaled dual-radius spherical arrays will validate the theoretical predictions and uncover practical considerations not captured in simulations.
f) The proposed framework can be tailored for applications such as mmWave and THz communications, massive MIMO systems, or satellite-based platforms where compact, high-gain, and directive antenna arrays are essential. Future research should explore application-specific optimizations within this framework.

References

[1] H.H. Chen, and S.C. Chan, "Adaptive Beamforming and DOA Estimation Using Uniform Concentric Spherical Arrays with Frequency Invariant Characteristics," *The Journal of VLSI Signal Processing Systems for Signal, Image, and Video Technology*, vol. 46, no. 1, pp. 15-34, 2007. [CrossRef] [Google Scholar] [Publisher Link]

[2] Shefeng Yan et al., "Optimal Modal Beamforming for Spherical Microphone Arrays," *IEEE Transactions on Audio, Speech, and Language Processing*, vol. 19, no. 2, pp. 361-371, 2011. [CrossRef] [Google Scholar] [Publisher Link]

[3] Nejem Huleihel, and Boaz Rafaely, "Spherical Array Processing for Acoustic Analysis Using Room Impulse Responses and Time-Domain Smoothing," *The Journal of the Acoustical Society of America*, vol. 6, no. 133, pp. 3995-4007, 2013. [CrossRef] [Google Scholar] [Publisher Link]

[4] Boaz Rafaely, Barak Weiss, and Eitan Bachmat, "Spatial Aliasing in Spherical Microphone Arrays," *IEEE Transactions on Signal Processing*, vol. 55, no. 3, pp. 1003-1010, 2007. [CrossRef] [Google Scholar] [Publisher Link]

[5] Haohai Sun et al., "Robust Localization of Multiple Sources in Reverberant Environments Using EB-ESPRIT with Spherical Microphone Arrays," *2011 IEEE International Conference on Acoustics, Speech and Signal Processing (ICASSP)*, Prague, Czech Republic, pp. 117-120, 2011. [CrossRef] [Google Scholar] [Publisher Link]

[6] Nicolas Epain, and Craig T. Jin, "Independent Component Analysis Using Spherical Microphone Arrays," *Acta Acustica United with Acustica*, vol. 98, no. 1, pp. 91-102, 2012. [CrossRef] [Google Scholar] [Publisher Link]

[7] Abhaya Parthy et al., "Comparison of the Measured and Theoretical Performance of a Broadband Circular Microphone Array," *The Journal of the Acoustical Society of America*, vol. 130, no. 6, pp. 3827-3837, 2011. [CrossRef] [Google Scholar] [Publisher Link]

[8] Jens Meyer, and Gary Elko, "A Highly Scalable Spherical Microphone Array Based on an Orthonormal Decomposition of the Soundfield," *2002 IEEE International Conference on Acoustics, Speech, and Signal Processing*, Orlando, FL, USA, pp. II-1781-II-1784, 2002. [CrossRef] [Google Scholar] [Publisher Link]

[9] Mahmoud Wagih, Alex S. Weddell, and Steve Beeby, "Omnidirectional Dual-Polarized Low-Profile Textile Rectenna with Over 50% Efficiency for Sub-μW/cm2 Wearable Power Harvesting," *IEEE Transactions on Antennas and Propagation*, vol. 69, no. 5, pp. 2522-2536, 2021. [CrossRef] [Google Scholar] [Publisher Link]

[10] Shanpu Shen, and Bruno Clerckx, "Beamforming Optimization for MIMO Wire-Less Power Transfer with Nonlinear Energy Harvesting: RF Combining Versus DC Combining," *IEEE Transactions on Wireless Communications*, vol. 20, no. 1, pp. 199-213, 2020. [CrossRef] [Google Scholar] [Publisher Link]

[11] Seung-Tae Khang et al., "Microwave Power Transfer with Optimal Number of Rectenna Arrays for Midrange Applications," *IEEE Antennas and Wireless Propagation Letters*, vol. 17, no. 1, pp. 155-159, 2018. [CrossRef] [Google Scholar] [Publisher Link]

[12] Tatsuki Matsunaga, Eisuke Nishiyama, and Ichihiko Toyoda, "5.8-GHz Stacked Differential Rectenna Suitable for Large-Scale Rectenna Arrays with DC Connection," *IEEE Transactions on Antennas and Propagation*, vol. 63, no. 12, pp. 5944-5949, 2015. [CrossRef] [Google Scholar] [Publisher Link]

[13] M. Fantuzzi et al., "An Orientation-Independent UHF Rectenna Array with a Unified Matching and Decoupling RF Network," *International Journal of Microwave and Wireless Technologies*, vol. 11, no. 5-6, pp. 490-500, 2019. [CrossRef] [Google Scholar] [Publisher Link]

[14] Azamat Bakytbekov et al., "Fully Printed 3D Cube-Shaped Multiband Fractal Rectenna for Ambient RF Energy Harvesting," *Nano Energy*, vol. 53, pp. 587-595, 2018. [CrossRef] [Google Scholar] [Publisher Link]

[15] Pooja Prajapat et al., "Near-Omnidirectional 3D Rectenna Array for Ambient Microwave Energy Harvesting," *2021 IEEE Indian Conference on Antennas and Propagation (InCAP)*, Jaipur, Rajasthan, India, pp. 747-749, 2021. [CrossRef] [Google Scholar] [Publisher Link]

[16] Sheng Wang, and Hong-Yeh Chang, "A 3D Rectenna with All-Polarization and Omnidirectional Capacity for IoT Applications," *2020 IEEE/MTT-S International Microwave Symposium (IMS)*, Los Angeles, CA, USA, pp. 1188-1190, 2020. [CrossRef] [Google Scholar] [Publisher Link]

[17] Manoj Kumar, Sundeep Kumar, and Ashwani Sharma, "A Compact 3-D Multisector Orientation Insensitive Wireless Power Transfer System," *IEEE Microwave and Wireless Technology Letters*, vol. 33, no. 3, pp. 363-366, 2023. [CrossRef] [Google Scholar] [Publisher Link]

[18] Hucheng Sun, and Wen Geyi, "A New Rectenna Using Beamwidth-Enhanced Antenna Array for RF Power Harvesting Applications," *IEEE Antennas and Wireless Propagation Letters*, vol. 16, pp. 1451-1454, 2016. [CrossRef] [Google Scholar] [Publisher Link]

[19] Arya Bangun, and Cosme Culotta-López, "Optimizing Sensing Matrices for Spherical Near-Field Antenna Measurements," *IEEE Transactions on Antennas and Propagation*, vol. 71, no. 2, pp. 1716-1724, 2023. [CrossRef] [Google Scholar] [Publisher Link]

[20] Hamid Reza Behjoo, Abbas Pirhadi, and Reza Asvadi, "Optimal Sampling in Spherical Near-Field Antenna Measurements by Utilizing the Information Content of Spherical Wave Harmonics," *IEEE Transactions on Antennas and Propagation*, vol. 70, no. 5, pp. 3762-3771, 2022. [CrossRef] [Google Scholar] [Publisher Link]

[21] Huapeng Zhao et al., “Skeletonization-Scheme-Based Adaptive Near Field Sampling for Radio Frequency Source Reconstruction,” *IEEE Internet of Things Journal*, vol. 6, no. 6, pp. 10219-10228, 2019. [CrossRef] [Google Scholar] [Publisher Link]

[22] Fernando Rodríguez Varela, Belén Galocha Iragüen, and Manuel Sierra-Castañer, “Under-Sampled Spherical Near-Field Antenna Measurements with Error Estimation,” *IEEE Transactions on Antennas and Propagation*, vol. 68, no. 8, pp. 6364-6371, 2020. [CrossRef] [Google Scholar] [Publisher Link]

[23] Arya Bangun, Arash Behboodi, and Rudolf Mathar, “Sensing Matrix Design and Sparse Recovery on the Sphere and the Rotation Group,” *IEEE Transactions on Signal Processing,* vol. 68, pp. 1439-1454, 2020. [CrossRef] [Google Scholar] [Publisher Link]

[24] B.Y. Duan et al., “Study of Optimization of Mechanical and Electrical Synthesis for the Antenna Structural System,” *Mechatronics*, vol. 4, no. 6, pp. 553-564, 1994. [CrossRef] [Google Scholar] [Publisher Link]

[25] Baoyan Duan, Congsi Wang, and Wei Wang, “Coupling Modeling for Functional Surface of Electronic Equipment,” *Chinese Journal of Mechanical Engineering*, vol. 30, no. 3, pp. 497-499, 2017. [CrossRef] [Google Scholar] [Publisher Link]